

Seismoelectric numerical simulation in 2D vertical transverse isotropic poroelastic medium

Tohti, Munirdin; Wang, Yibo; Slob, Evert; Zheng, Yikang; Chang, Xu; Yao, Yi

DOI

[10.1111/1365-2478.12958](https://doi.org/10.1111/1365-2478.12958)

Publication date

2020

Document Version

Final published version

Published in

Geophysical Prospecting

Citation (APA)

Tohti, M., Wang, Y., Slob, E., Zheng, Y., Chang, X., & Yao, Y. (2020). Seismoelectric numerical simulation in 2D vertical transverse isotropic poroelastic medium. *Geophysical Prospecting*, 68(6), 1927-1943. <https://doi.org/10.1111/1365-2478.12958>

Important note

To cite this publication, please use the final published version (if applicable). Please check the document version above.

Copyright

Other than for strictly personal use, it is not permitted to download, forward or distribute the text or part of it, without the consent of the author(s) and/or copyright holder(s), unless the work is under an open content license such as Creative Commons.

Takedown policy

Please contact us and provide details if you believe this document breaches copyrights. We will remove access to the work immediately and investigate your claim.

Green Open Access added to TU Delft Institutional Repository

'You share, we take care!' – Taverne project

<https://www.openaccess.nl/en/you-share-we-take-care>

Otherwise as indicated in the copyright section: the publisher is the copyright holder of this work and the author uses the Dutch legislation to make this work public.

Seismoelectric numerical simulation in 2D vertical transverse isotropic poroelastic medium

Munirdin Tohti^{1,2,3}, Yibo Wang^{1,3*}, Evert Slob⁴, Yikang Zheng^{1,3}, Xu Chang^{1,3} and Yi Yao^{1,2,3}

¹Key Laboratory of Petroleum Resource Research, Institute of Geology and Geophysics, Chinese Academy of Sciences, Beijing, 100029, China, ²University of Chinese Academy of Sciences, Beijing, 100049, China, ³Innovation Academy for Earth Science, CAS, Beijing, 100029, China, and ⁴Department of Geoscience & Engineering, Delft University of Technology, Delft, 2628 CD, The Netherlands

Received August 2019, revision accepted March 2020

ABSTRACT

Seismoelectric coupling in an electric isotropic and elastic anisotropic medium is developed using a primary–secondary formulation. The anisotropy is of vertical transverse isotropic type and concerns only the poroelastic parameters. Based on our finite difference time domain algorithm, we solve the seismoelectric response to an explosive source. The seismic wavefields are computed as the primary field. The electric field is then obtained as a secondary field by solving the Poisson equation for the electric potential. To test our numerical algorithm, we compared our seismoelectric numerical results with analytical results obtained from Pride's equation. The comparison shows that the numerical solution gives a good approximation to the analytical solution. We then simulate the seismoelectric wavefields in different models. Simulated results show that four types of seismic waves are generated in anisotropic poroelastic medium. These are the fast and slow longitudinal waves and two separable transverse waves. All of these seismic waves generate coseismic electric fields in a homogenous anisotropic poroelastic medium. The tortuosity has an effect on the propagation of the slow longitudinal wave. The snapshot of the slow longitudinal wave has an oval shape when the tortuosity is anisotropic, whereas it has a circular shape when the tortuosity is isotropic. In terms of the Thomsen parameters, the radiation anisotropy of the fast longitudinal wave is more sensitive to the value of ϵ , while the radiation anisotropy of the transverse wave is more sensitive to the value of δ .

Key words: Poroelastic medium, Seismoelectric coupling, Thomsen parameters, Vertical transverse isotropy.

INTRODUCTION

Seismic waves can be converted into electromagnetic (EM) fields, and *vice versa*, in a porous medium due to the electrokinetic effect (Ivanov, 1939; Martner and Sparks, 1959; Schoemaker *et al.*, 2012). The mutual conversion between the seismic waves and EM fields can be referred to as 'seismoelectric' coupling phenomena, which has been validated by field and laboratory experiments (Zhu *et al.*, 1999; Garam-

bois and Dietrich, 2001; Bordes *et al.*, 2006; Thompson *et al.*, 2007; Zhu *et al.*, 2008; Schakel *et al.*, 2011a,b, 2012; Zhu and Toksöz, 2013).

A set of governing equations that describe the propagation of seismoelectric waves has been derived by Pride (1994). The governing equations consist of coupling between Maxwell's equation that describe the propagation and diffusion of electromagnetic fields and Biot's equation that describe the propagation of seismic waves in poroelastic medium (Biot, 1956a, 1956b). An alternative electrokinetic formulation that describes the wave propagation in unsaturated porous media has been proposed by Revil and Linde (2006) and Revil and Mahardika (2013).

[Correction added on 26 June 2020, after first online publication: The symbol for porosity has been corrected to Φ in this version.]

*E-mail: wangyibo@mail.iggcas.ac.cn

Two types of coupled seismoelectric signals have become the topic of research. The first one is the coseismic EM field that travels at the same speed as seismic wave (Haartsen and Pride, 1997; Gao and Hu, 2010). The coseismic signal is generated by the seismic signal while it travels through the medium. The second one is referred to as seismoelectric interface response, which is generated by mechanic waves when it encounters an interface between two different porous media or an interface that separates a porous medium and another kind of medium (e.g. a fluid) (Mikhailov *et al.*, 1997; White and Zhou, 2006).

Numerical modelling and laboratory experiments have been carried out to investigate the seismoelectric signals in different media. Green's functions have been derived for a homogenous space (Pride and Haartsen, 1996; Slob and Mulder, 2016), horizontally stratified medium (Haartsen and Pride, 1997; Garambois and Dietrich, 2002, Gao and Hu, 2009) and in a homogeneous half space with excitation by a finite fault (Ren *et al.*, 2011, 2016). Gao *et al.* (2017a,b) developed analytical formulation of quasi-static seismoelectric signals. Modelling 2D seismoelectric waves with finite difference frequency domain algorithm has been derived by Gao *et al.* (2018). Seismoelectric couplings in a poroelastic medium containing two immiscible fluid phases has been analysed by Jardani and Revil (2015). Haines and Pride (2006) derived quasi-static electromagnetic approximation of Pride's equation by ignoring the electro-osmotic feedback and simulated the seismoelectric signals on a grid. Finite element modelling of seismoelectric waves has been performed by Zyserman *et al.* (2010). Zhu and Toksoz (2015) carried out laboratory experiments on porous samples to analyse the effect of anisotropic permeability on the coupling coefficient.

All of the numerical simulations that have been published before are analytical or deal only with isotropic media. However, a vertical transverse isotropic (VTI) medium is generally considered to be common for shale formations and layered media (Thomsen, 1986; Tsvankin, 1996, 1997; Pooladi *et al.*, 2017). In order to study the seismoelectric response of an actual geological structure, especially the horizontal thin bed sequence, it is necessary to perform a numerical simulation in the VTI medium and analyse the effect of medium anisotropy on the propagation of seismoelectric waves.

In this paper, we derive seismoelectric coupling equations for 2D VTI poroelastic media under the assumption that the poroelastic medium is electrically isotropic but has elastic anisotropy. We use the finite difference time domain (FDTD) algorithm to compute the seismic waves in the first step by ignoring the converted electromagnetic wave's influence on the

propagation of seismic signals. We then calculate the electric signals resulting from the seismic signals by solving the Poisson equation of electric potential with a mechanical source term and the coupling coefficient. We design several models to simulate their seismoelectric response. We test our numerical algorithm by comparing the numerical and analytical solutions. Then we compute snapshots for different models and analyse the effect of the medium anisotropy on the propagation of seismoelectric waves. Finally, we test the parallelizing efficiency of our FDTD simulation code.

COUPLING EQUATIONS IN ANISOTROPIC POROELASTIC MEDIUM

Pride (1994) has derived the full set of governing equations for the coupled electromagnetic and seismic response in a homogeneous porous medium. In Pride's model, both the solid grains and all the macroscopic constitutive laws are assumed to be isotropic, piezo or other anisotropic effects are absent (Pride, 1994; Slob and Mulder, 2016). Haines and Pride (2006) made the quasi-static electromagnetic approximation to the Pride's model and obtained a set of reduced equations. Due to the presence of aligned microcracks, fractures and tortuosity of the rocks, porous media often appear to be anisotropic. In order to investigate the seismoelectric response of such medium, we assume the porous medium to be electrically isotropic but to have elastic anisotropy. Based on previous achievements (Biot, 1955, 1956a,b, 1962; Carcione, 1995; Yang and Zhang, 2002; Haines and Pride, 2006; Sharma, 2007; Slob and Mulder, 2016; Gilbert and Shoushani, 2017), we develop the quasi-static electromagnetic coupling equations describing the seismoelectric wave propagation in a 2D vertical transverse isotropic (VTI) medium, expressed as

$$\frac{\partial v_1}{\partial t} = \frac{\tilde{\rho}_f}{\rho\tilde{\rho}_f - \rho_f^2} \left(\frac{\partial T_{11}}{\partial x_1} + \frac{\partial T_{12}}{\partial x_2} \right) + \frac{\rho_f}{\rho\tilde{\rho}_f - \rho_f^2} \frac{\eta_f}{k_1} w_1 + \frac{\rho_f}{\rho\tilde{\rho}_f - \rho_f^2} \frac{\partial P}{\partial x_1} \quad (1)$$

$$\frac{\partial v_2}{\partial t} = \frac{\tilde{\rho}_f}{\rho\tilde{\rho}_f - \rho_f^2} \left(\frac{\partial T_{12}}{\partial x_1} + \frac{\partial T_{22}}{\partial x_2} \right) + \frac{\rho_f}{\rho\tilde{\rho}_f - \rho_f^2} \frac{\eta_f}{k_2} w_2 + \frac{\rho_f}{\rho\tilde{\rho}_f - \rho_f^2} \frac{\partial P}{\partial x_2} \quad (2)$$

$$\frac{\partial w_1}{\partial t} = -\frac{\rho_f}{\rho\tilde{\rho}_f - \rho_f^2} \left(\frac{\partial T_{11}}{\partial x_1} + \frac{\partial T_{12}}{\partial x_2} \right) - \frac{\rho}{\rho\tilde{\rho}_f - \rho_f^2} \frac{\eta_f}{k_1} w_1 - \frac{\rho}{\rho\tilde{\rho}_f - \rho_f^2} \frac{\partial P}{\partial x_1} \quad (3)$$

$$\frac{\partial w_2}{\partial t} = -\frac{\rho_f}{\rho \tilde{\rho}_f - \rho_f^2} \left(\frac{\partial T_{12}}{\partial x_1} + \frac{\partial T_{22}}{\partial x_2} \right) - \frac{\rho}{\rho \tilde{\rho}_f - \rho_f^2} \frac{\eta_f}{k_2} w_2 - \frac{\rho}{\rho \tilde{\rho}_f - \rho_f^2} \frac{\partial P}{\partial x_2} \quad (4)$$

$$\frac{\partial T_{11}}{\partial t} = \tilde{C}_{11} \frac{\partial v_1}{\partial x_1} + \tilde{C}_{12} \frac{\partial v_2}{\partial x_2} + C_1 \frac{\partial w_1}{\partial x_1} + C_1 \frac{\partial w_2}{\partial x_2} \quad (5)$$

$$\frac{\partial T_{22}}{\partial t} = \tilde{C}_{12} \frac{\partial v_1}{\partial x_1} + \tilde{C}_{22} \frac{\partial v_2}{\partial x_2} + C_2 \frac{\partial w_1}{\partial x_1} + C_2 \frac{\partial w_2}{\partial x_2} \quad (6)$$

$$\frac{\partial T_{12}}{\partial t} = \tilde{C}_{66} \frac{\partial v_2}{\partial x_1} + \tilde{C}_{66} \frac{\partial v_1}{\partial x_2} \quad (7)$$

$$-\frac{\partial P}{\partial t} = C_1 \frac{\partial v_1}{\partial x_1} + C_2 \frac{\partial v_2}{\partial x_2} + M \frac{\partial w_1}{\partial x_1} + M \frac{\partial w_2}{\partial x_2} \quad (8)$$

$$\nabla \cdot (\sigma \nabla \varphi) = \frac{\partial}{\partial x_i} \left(\frac{\eta_f L_i}{k_i} \right) w_i \quad (9)$$

$$E_1 = -\frac{\partial \varphi}{\partial x_1} \quad (10)$$

$$E_2 = -\frac{\partial \varphi}{\partial x_2}, \quad (11)$$

where ρ_f is the mass density of the fluid; ρ is the saturated rock density, given by $\rho = (1 - \Phi)\rho_s + \Phi\rho_f$, in which ρ_s represents the density of the solid, Φ represents the porosity; $\tilde{\rho}_f$ is the effective density of the fluid, given by $\tilde{\rho}_f = \frac{\mathcal{T}\rho_f}{\Phi}$, in which \mathcal{T} is the tortuosity; when the tortuosity is anisotropic, the value of the $\tilde{\rho}_f$ will be different in vertical and horizontal directions; w_i represents the relative velocity (fluid relative to the solid) vector component ($i = 1, 2$), given by $w_i = \Phi(v_i^f - v_i)$, in which v_i and v_i^f represent the velocity vector components in the solid and fluid, respectively; η_f is the fluid viscosity; L is the static coupling coefficient, given by $L = -\frac{\mu\Phi\varepsilon_0\varepsilon_{RF}}{\mathcal{T}\eta_f}$, in which μ is zeta potential, ε_0 is free-space electric permittivity, ε_{RF} is relative permittivity of fluid; E_i is the vector component of the electric field; φ is electric potential; σ is conductivity of the porous medium; T_{ij} is the bulk stress tensor component ($j = 1, 2$); P is the acoustic pressure; M and C_i denote the stiffness parameters of the porous solid, given by $M = \frac{k_f}{\Phi(1+\lambda)}$, where λ is given by $\lambda = \frac{k_f(1-\Phi)k_s - k_{fr}}{\Phi + k_s^2}$; k_f , k_s , k_{fr} denote moduli of the fluid, framework of grains and skeleton grains, respectively. A vector component of the static permeability is denoted by k_i ; subscript number i denotes the vertical direction when $i = 1$, and denotes the horizontal direction when $i = 2$.

\tilde{C}_{11} , \tilde{C}_{22} , \tilde{C}_{12} , \tilde{C}_{66} are undrained elastic components, the relations with drained elastic components are given by (Carcione, 1995)

$$\tilde{C}_{11} = C_{11} + \alpha_1 C_1 \quad (12)$$

$$\tilde{C}_{22} = C_{22} + \alpha_2 C_2 \quad (13)$$

$$\tilde{C}_{12} = C_{12} + \alpha_1 \alpha_2 M \quad (14)$$

$$\tilde{C}_{66} = C_{66}. \quad (15)$$

The relationship between the stiffness parameters are given by (Carcione, 1995)

$$C_1 = \alpha_1 M \quad (16)$$

$$C_2 = \alpha_2 M, \quad (17)$$

where the effective coefficients are given by (Carcione, 1995)

$$\alpha_1 = 1 - \frac{C_{11} + 2C_{12}}{3k_s} \quad (18)$$

$$\alpha_2 = 1 - \frac{C_{22} + 2C_{12}}{3k_s}. \quad (19)$$

Equations (1)–(11) are the coupling equations under the quasi-static electric approximation that are used to simulate the seismoelectric response in a 2D VTI medium. It can be seen from these coupling equations that the particle velocities are related to elastic components of stiffness tensor C_{11} , C_{22} , C_{12} , C_{66} . The stiffness tensor of 3D VTI medium is given by

$$\begin{bmatrix} C_{11} & C_{12} & C_{12} & 0 & 0 & 0 \\ C_{12} & C_{22} & C_{22} - 2C_{44} & 0 & 0 & 0 \\ C_{12} & C_{22} - 2C_{44} & C_{22} & 0 & 0 & 0 \\ 0 & 0 & 0 & C_{44} & 0 & 0 \\ 0 & 0 & 0 & 0 & C_{66} & 0 \\ 0 & 0 & 0 & 0 & 0 & C_{66} \end{bmatrix}. \quad (20)$$

According to the previous research results (Thomsen, 1986), the anisotropic parameters are used to describe the anisotropy of the elastic medium, which are given by

$$\varepsilon = \frac{C_{22} - C_{11}}{2C_{11}}, \quad \gamma = \frac{C_{44} - C_{66}}{2C_{66}},$$

$$\delta = \frac{(C_{12} + C_{66})^2 - (C_{11} - C_{66})^2}{2C_{11}(C_{11} - C_{66})},$$

$$\alpha = \sqrt{\frac{C_{11}}{\rho}}, \quad \beta = \sqrt{\frac{C_{66}}{\rho}}, \quad (21)$$

[Corrections made on 8 June 2020, after first online publication: The denominator for and the numerator for

Equation (21) were previously incorrect and these have now been updated in this version.]

where α and β are the phase velocity of the longitudinal and transverse waves in the direction of the axis of the symmetry. In a 2D VTI medium, formula (20) can be converted into the following form:

$$\begin{bmatrix} C_{11} & C_{12} & 0 \\ C_{12} & C_{22} & 0 \\ 0 & 0 & C_{66} \end{bmatrix}. \tag{22}$$

NUMERICAL IMPLEMENTATION

Finite-difference methods are one of the numerical modelling techniques for solving partial differential equations. In this numerical modelling scheme, we use first-order central-difference approximation (Yee, 1966; Virieux, 1984) to the space and time partial derivatives. We use sponge layer absorbing boundary conditions to suppress the reflections of the seismic waves from the boundaries (Petropoulos *et al.*, 1998). The finite difference time domain (FDTD) seismic coupling equations are obtained from equations (1)–(11) by approximating all derivatives based on the following principle:

$$\frac{\partial f}{\partial x}(x) \approx \frac{f(x + \frac{\Delta x}{2}) - f(x - \frac{\Delta x}{2})}{\Delta x}. \tag{23}$$

Following equation (23), the final FDTD discretizing form are given by

$$\begin{aligned} v_1(x_1, x_2, t + \Delta t) &= v_1(x_1, x_2, t) \\ &+ \frac{\Delta t}{\Delta x} \times \left[\frac{\tilde{\rho}_f}{\rho \tilde{\rho}_f - \rho_f^2} \left(T_{11} \left(x_1 + \frac{\Delta x}{2}, x_2, t + \frac{\Delta t}{2} \right) \right. \right. \\ &- T_{11} \left(x_1 - \frac{\Delta x}{2}, x_2, t + \frac{\Delta t}{2} \right) + T_{12} \left(x_1, x_2 + \frac{\Delta x}{2}, t + \frac{\Delta t}{2} \right) \\ &- T_{12} \left(x_1, x_2 - \frac{\Delta x}{2}, t + \frac{\Delta t}{2} \right) \left. \right] + \frac{\rho_f}{\rho \tilde{\rho}_f - \rho_f^2} \\ &\left(P \left(x_1 + \frac{\Delta x}{2}, x_2, t + \frac{\Delta t}{2} \right) - P \left(x_1 - \frac{\Delta x}{2}, x_2, t + \frac{\Delta t}{2} \right) \right) \\ &+ \Delta t \frac{\rho_f}{\rho \tilde{\rho}_f - \rho_f^2} \frac{\eta_f}{k_1} w_1(x_1, x_2, t) \end{aligned} \tag{24}$$

$$\begin{aligned} v_2(x_1, x_2, t + \Delta t) &= v_2(x_1, x_2, t) \\ &+ \frac{\Delta t}{\Delta x} \times \left[\frac{\tilde{\rho}_f}{\rho \tilde{\rho}_f - \rho_f^2} \left(T_{12} \left(x_1 + \frac{\Delta x}{2}, x_2, t + \frac{\Delta t}{2} \right) \right. \right. \\ &- T_{12} \left(x_1 - \frac{\Delta x}{2}, x_2, t + \frac{\Delta t}{2} \right) + T_{22} \left(x_1, x_2 + \frac{\Delta x}{2}, t + \frac{\Delta t}{2} \right) \\ &- T_{22} \left(x_1, x_2 - \frac{\Delta x}{2}, t + \frac{\Delta t}{2} \right) \left. \right] \end{aligned}$$

$$\begin{aligned} &- T_{22} \left(x_1, x_2 - \frac{\Delta x}{2}, t + \frac{\Delta t}{2} \right) \left. \right] + \frac{\rho_f}{\rho \tilde{\rho}_f - \rho_f^2} \\ &\left(P \left(x_1, x_2 + \frac{\Delta x}{2}, t + \frac{\Delta t}{2} \right) - P \left(x_1, x_2 - \frac{\Delta x}{2}, t + \frac{\Delta t}{2} \right) \right) \\ &+ \Delta t \frac{\rho_f}{\rho \tilde{\rho}_f - \rho_f^2} \frac{\eta_f}{k_2} w_2(x_1, x_2, t) \end{aligned} \tag{25}$$

$$\begin{aligned} w_1(x_1, x_2, t + \Delta t) &= w_1(x_1, x_2, t) \\ &- \frac{\Delta t}{\Delta x} \times \left[\frac{\rho_f}{\rho \tilde{\rho}_f - \rho_f^2} \left(T_{11} \left(x_1 + \frac{\Delta x}{2}, x_2, t + \frac{\Delta t}{2} \right) \right. \right. \\ &- T_{11} \left(x_1 - \frac{\Delta x}{2}, x_2, t + \frac{\Delta t}{2} \right) + T_{12} \left(x_1, x_2 + \frac{\Delta x}{2}, t + \frac{\Delta t}{2} \right) \\ &- T_{12} \left(x_1, x_2 - \frac{\Delta x}{2}, t + \frac{\Delta t}{2} \right) \left. \right] + \frac{\rho}{\rho \tilde{\rho}_f - \rho_f^2} \\ &\left(P \left(x_1 + \frac{\Delta x}{2}, x_2, t + \frac{\Delta t}{2} \right) - P \left(x_1 - \frac{\Delta x}{2}, x_2, t + \frac{\Delta t}{2} \right) \right) \\ &- \Delta t \frac{\rho}{\rho \tilde{\rho}_f - \rho_f^2} \frac{\eta_f}{k_1} w_1(x_1, x_2, t) \end{aligned} \tag{26}$$

$$\begin{aligned} w_2(x_1, x_2, t + \Delta t) &= w_2(x_1, x_2, t) \\ &- \frac{\Delta t}{\Delta x} \times \left[\frac{\rho_f}{\rho \tilde{\rho}_f - \rho_f^2} \left(T_{12} \left(x_1 + \frac{\Delta x}{2}, x_2, t + \frac{\Delta t}{2} \right) \right. \right. \\ &- T_{12} \left(x_1 - \frac{\Delta x}{2}, x_2, t + \frac{\Delta t}{2} \right) + T_{22} \left(x_1, x_2 + \frac{\Delta x}{2}, t + \frac{\Delta t}{2} \right) \\ &- T_{22} \left(x_1, x_2 - \frac{\Delta x}{2}, t + \frac{\Delta t}{2} \right) \left. \right] + \frac{\rho}{\rho \tilde{\rho}_f - \rho_f^2} \\ &\left(P \left(x_1, x_2 + \frac{\Delta x}{2}, t + \frac{\Delta t}{2} \right) - P \left(x_1, x_2 - \frac{\Delta x}{2}, t + \frac{\Delta t}{2} \right) \right) \\ &- \Delta t \frac{\rho}{\rho \tilde{\rho}_f - \rho_f^2} \frac{\eta_f}{k_2} w_2(x_1, x_2, t) \end{aligned} \tag{27}$$

$$\begin{aligned} T_{11}(x_1, x_2, t + \Delta t) &= T_{11}(x_1, x_2, t) \\ &+ \frac{\Delta t}{\Delta x} \times \left[\tilde{C}_{11}(x_1, x_2) \left[v_1 \left(x_1 + \frac{\Delta x}{2}, x_2, t + \frac{\Delta t}{2} \right) \right. \right. \\ &- v_1 \left(x_1 - \frac{\Delta x}{2}, x_2, t + \frac{\Delta t}{2} \right) \left. \right] \\ &+ \tilde{C}_{12}(x_1, x_2) \left[v_2 \left(x_1, x_2 + \frac{\Delta x}{2}, t + \frac{\Delta t}{2} \right) \right. \\ &- v_2 \left(x_1, x_2 - \frac{\Delta x}{2}, t + \frac{\Delta t}{2} \right) \left. \right] \\ &+ C_1(x_1, x_2) \left[w_1 \left(x_1 + \frac{\Delta x}{2}, x_2, t + \frac{\Delta t}{2} \right) \right. \end{aligned}$$

$$\begin{aligned}
 & -w_1 \left(x_1 - \frac{\Delta x}{2}, x_2, t + \frac{\Delta t}{2} \right) \\
 & + C_1(x_1, x_2) \left[w_2 \left(x_1, x_2 + \frac{\Delta x}{2}, t + \frac{\Delta t}{2} \right) \right. \\
 & \left. - w_2 \left(x_1, x_2 - \frac{\Delta x}{2}, t + \frac{\Delta t}{2} \right) \right] \quad (28)
 \end{aligned}$$

$$\begin{aligned}
 T_{22}(x_1, x_2, t + \Delta t) &= T_{22}(x_1, x_2, t) \\
 & + \frac{\Delta t}{\Delta x} \times \left[\tilde{C}_{12}(x_1, x_2) \left[v_1 \left(x_1 + \frac{\Delta x}{2}, x_2, t + \frac{\Delta t}{2} \right) \right. \right. \\
 & \left. \left. - v_1 \left(x_1 - \frac{\Delta x}{2}, x_2, t + \frac{\Delta t}{2} \right) \right] \right. \\
 & + \tilde{C}_{22}(x_1, x_2) \left[v_2 \left(x_1, x_2 + \frac{\Delta x}{2}, t + \frac{\Delta t}{2} \right) \right. \\
 & \left. - v_2 \left(x_1, x_2 - \frac{\Delta x}{2}, t + \frac{\Delta t}{2} \right) \right] \\
 & + C_2(x_1, x_2) \left[w_1 \left(x_1 + \frac{\Delta x}{2}, x_2, t + \frac{\Delta t}{2} \right) \right. \\
 & \left. - w_1 \left(x_1 - \frac{\Delta x}{2}, x_2, t + \frac{\Delta t}{2} \right) \right] \\
 & + C_2(x_1, x_2) \left[w_2 \left(x_1, x_2 + \frac{\Delta x}{2}, t + \frac{\Delta t}{2} \right) \right. \\
 & \left. - w_2 \left(x_1, x_2 - \frac{\Delta x}{2}, t + \frac{\Delta t}{2} \right) \right] \quad (29)
 \end{aligned}$$

$$\begin{aligned}
 T_{12}(x_1, x_2, t + \Delta t) &= T_{12}(x_1, x_2, t) \\
 & + \frac{\Delta t}{\Delta x} \times \left[\tilde{C}_{66}(x_1, x_2) \left[v_2 \left(x_1 + \frac{\Delta x}{2}, x_2, t + \frac{\Delta t}{2} \right) \right. \right. \\
 & \left. \left. - v_2 \left(x_1 - \frac{\Delta x}{2}, x_2, t + \frac{\Delta t}{2} \right) \right] \right. \\
 & + \tilde{C}_{66}(x_1, x_2) \left[v_1 \left(x_1, x_2 + \frac{\Delta x}{2}, t + \frac{\Delta t}{2} \right) \right. \\
 & \left. \left. - v_1 \left(x_1, x_2 - \frac{\Delta x}{2}, t + \frac{\Delta t}{2} \right) \right] \right] \quad (30)
 \end{aligned}$$

$$\begin{aligned}
 P(x_1, x_2, t + \Delta t) &= P(x_1, x_2, t) \\
 & - \frac{\Delta t}{\Delta x} \times \left[C_1(x_1, x_2) \left[v_1 \left(x_1 + \frac{\Delta x}{2}, x_2, t + \frac{\Delta t}{2} \right) \right. \right. \\
 & \left. \left. - v_1 \left(x_1 - \frac{\Delta x}{2}, x_2, t + \frac{\Delta t}{2} \right) \right] \right. \\
 & \left. + C_2(x_1, x_2) \left[v_2 \left(x_1, x_2 + \frac{\Delta x}{2}, t + \frac{\Delta t}{2} \right) \right. \right.
 \end{aligned}$$

$$\begin{aligned}
 & \left. - v_2 \left(x_1, x_2 - \frac{\Delta x}{2}, t + \frac{\Delta t}{2} \right) \right] \\
 & + M(x_1, x_2) \left[w_1 \left(x_1 + \frac{\Delta x}{2}, x_2, t + \frac{\Delta t}{2} \right) \right. \\
 & \left. - w_1 \left(x_1 - \frac{\Delta x}{2}, x_2, t + \frac{\Delta t}{2} \right) \right] \\
 & + M(x_1, x_2) \left[w_2 \left(x_1, x_2 + \frac{\Delta x}{2}, t + \frac{\Delta t}{2} \right) \right. \\
 & \left. - w_2 \left(x_1, x_2 - \frac{\Delta x}{2}, t + \frac{\Delta t}{2} \right) \right] \quad (31)
 \end{aligned}$$

$$\begin{aligned}
 \varphi(x_1, x_2, t) &= \frac{1}{4} \left[\varphi \left(x_1 + \frac{\Delta x}{2}, x_2, t \right) \right. \\
 & + \varphi \left(x_1 - \frac{\Delta x}{2}, x_2, t \right) + \varphi \left(x_1, x_2 + \frac{\Delta x}{2}, t \right) \\
 & + \varphi \left(x_1, x_2 - \frac{\Delta x}{2}, t \right) - \Delta x \cdot \frac{L_1 \eta_f}{k_1 \sigma} \\
 & \left. \left[w_1 \left(x_1 + \frac{\Delta x}{2}, x_2, t \right) - w_1 \left(x_1 - \frac{\Delta x}{2}, x_2, t \right) \right] \right. \\
 & \left. - \Delta x \frac{L_2 \eta_f}{k_2 \sigma} \left[w_2 \left(x_1, x_2 + \frac{\Delta x}{2}, t \right) \right. \right. \\
 & \left. \left. - w_2 \left(x_1, x_2 - \frac{\Delta x}{2}, t \right) \right] \right] \quad (32)
 \end{aligned}$$

$$E_1(x_1, x_2, t) = - \frac{\varphi \left(x_1 + \frac{\Delta x}{2}, x_2, t \right) - \varphi \left(x_1 - \frac{\Delta x}{2}, x_2, t \right)}{\Delta x} \quad (33)$$

$$E_2(x_1, x_2, t) = - \frac{\varphi \left(x_1, x_2 + \frac{\Delta x}{2}, t \right) - \varphi \left(x_1, x_2 - \frac{\Delta x}{2}, t \right)}{\Delta x} \quad (34)$$

In equations (24)–(34), Δx and Δt are the spatial and time steps used to approximate spatial and time derivatives according to equation (23). Based on the above FDTD discretized equations, we parallelize the modelling program by using Open MP to improve the computation efficiency.

NUMERICAL RESULTS

Verification of algorithm

In order to validate the correctness of our numerical modelling algorithm, in the first step, we set the Thomsen anisotropic parameters as $\varepsilon = 0$, $\gamma = 0$, $\delta = 0$ to model an isotropic medium.

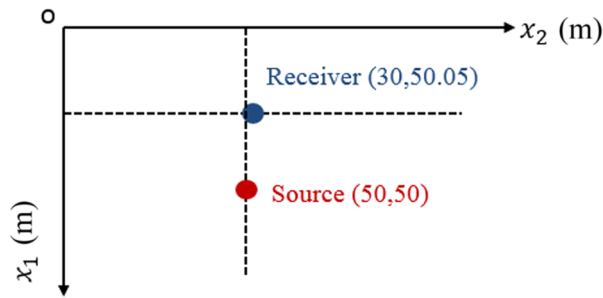


Figure 1 Configuration of the receiver and source location.

We use the 2D equivalent of the 3D analytical solution from Slob and Mulder (2016) to test our modelling code. We use a 1 kHz Ricker wavelet as the source time function and 2000×2000 grid points with grid spacing of 0.05 m in both directions, and the time step is 0.01 milliseconds. We put an explosive source at the centre of simulation model and receive the signal at a receiver R. The coordinates of the receiver and source are shown in Fig. 1.

In all examples we model the waves and fields in homogeneous media. We use Model A from Table 1 to test the code. The comparison of the finite difference time domain (FDTD) results with the analytical results are shown in Fig. 2. As we can see from comparison results, the FDTD numerical solution has a good match with the analytical solution. We also calculate the relative errors in each field at the maximum amplitude. The relative errors of the numerical solution of the

V1, V2, W1, W2, E1, E2 to the analytical solution are 0.31%, 0.32%, 0.35%, 0.38%, 0.22%, 0.22%, respectively.

Numerical examples

In this section, we compute the seismoelectric response to an explosive source, including snapshots of solid velocity, relative velocity and electric field. We also use the Ricker wavelet as the time source signature with centre frequency of 1 kHz. The simulation dimension of the model is 2000×2000 grid points with grid spacing of 0.05 m in both directions, and the time step is 0.01 milliseconds. We arrange 1000 receivers in the horizontal direction above the source, and the minimum distance between the receivers and source location is 20 m.

First, we simulate Model A, whose parameters are shown in Table 1. We show the computed snapshots at 12 milliseconds in Fig. 3. We observe that the explosive source excites only the fast (P_f) and slow (P_s) longitudinal waves in an isotropic poroelastic medium. Both waves generate only the coseismic electric signal. The fast longitudinal wave is similar to the longitudinal wave that is generated in an elastic medium. However, the slow longitudinal wave has different characteristics depending on the fluid properties. The slow longitudinal wave appears at the source in a static mode, as shown in Fig. 3, in which E_{P_f} and E_{P_s} are the coseismic fields inside the P_f and P_s waves. This is because the slow longitudinal wave propagates slowly under the effect of fluid viscosity.

Table 1 Model parameters used in numerical simulations

Parameter's Symbol	Model A	Model B	Model C	Model D	Model E	Model F
σ (S m^{-1})	9.3×10^{-4}					
ρ_s (kg/m^3)	2700	2700	2700	2700	2700	2700
ρ_f (kg/m^3)	1000	1000	1000	1000	1000	1000
\mathcal{T}_1	3	3	3	3	3	3
\mathcal{T}_2	3	3	3	3	3	6
k_1 (m^2)	1.3×10^{-12}					
k_2 (m^2)	1.3×10^{-12}	6.0×10^{-12}				
L_1 ($\text{FV}/(\text{mPas})$)	6.8×10^{-9}	6.8×10^{-9}	6.8×10^{-9}	6.8×10^{-9}	6.8×10^{-7}	6.8×10^{-7}
L_2 ($\text{FV}/(\text{mPas})$)	6.8×10^{-9}	6.8×10^{-9}	6.8×10^{-9}	6.8×10^{-9}	6.8×10^{-7}	3.4×10^{-7}
η_f (Pas)	10^{-3}	10^{-3}	10^{-3}	10^{-3}	10^{-5}	10^{-5}
k_s (GPa)	40	40	40	40	40	40
M	6.6	6.6	6.6	6.6	6.6	6.6
C_{11} (GPa)	21.35	21.35	21.35	21.35	21.35	21.35
C_{22} (GPa)	21.35	23.485	27.755	27.755	27.755	27.755
C_{12} (GPa)	3.35	5.3268	5.3268	0.9894	0.9894	0.9894
C_{66} (GPa)	9	7.2	7.2	7.2	7.2	7.2
ε	0	0.05	0.15	0.15	0.15	0.15
δ	0	-0.072	-0.072	-0.22	-0.22	-0.22
γ	0	0.125	0.125	0.125	0.125	0.125

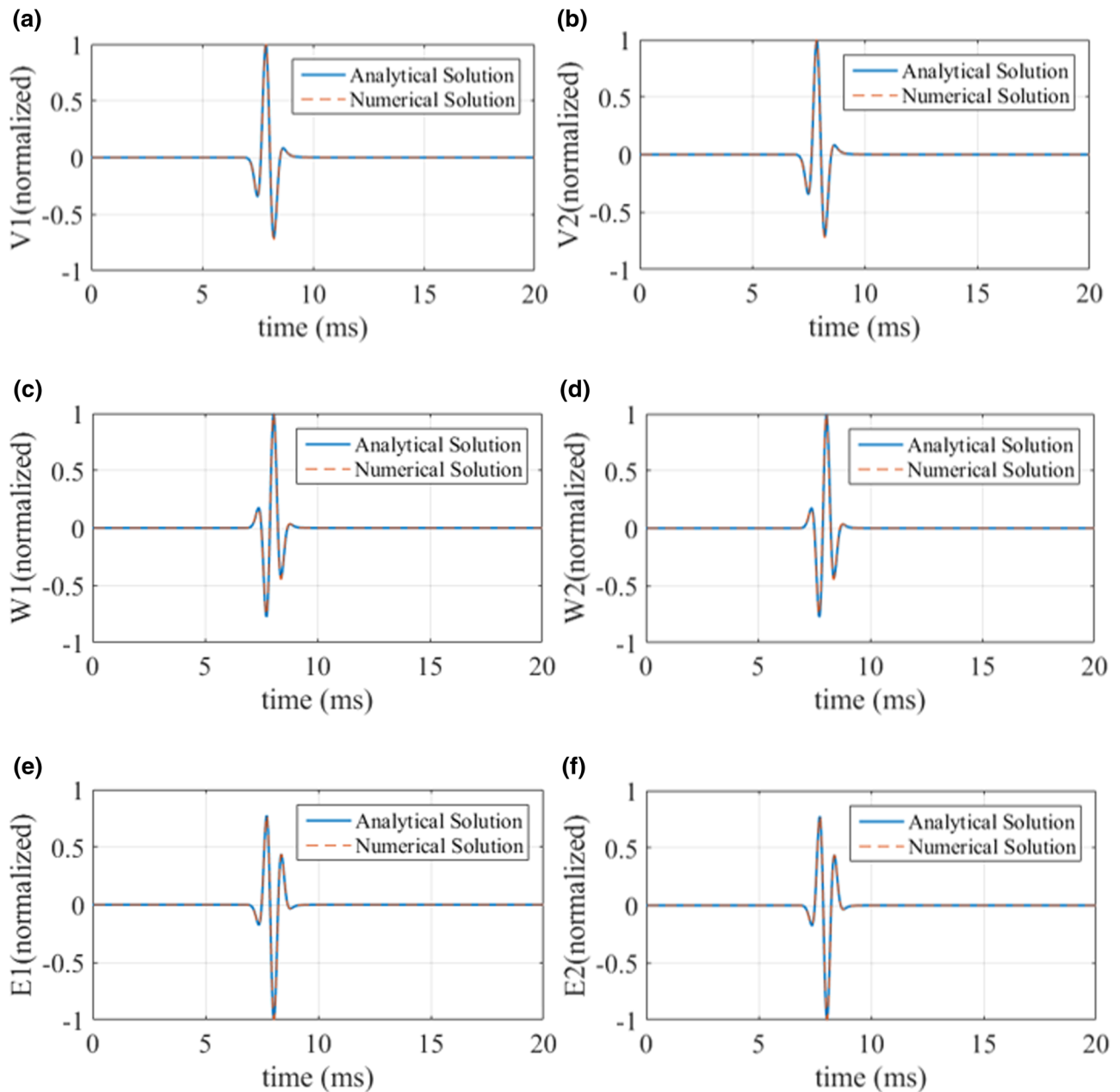


Figure 2 Comparison of seismoelectric waves between analytical solution and numerical solution: (a) solid velocity component on the vertical direction, (b) solid velocity component on the horizontal direction, (c) relative velocity component on the vertical direction, (d) relative velocity component on the horizontal direction, (e) electric field component on the vertical direction and (f) electric field component on the horizontal direction.

In order to understand the propagation characteristics of seismoelectric waves in the anisotropic poroelastic medium, we analyse the effect of viscosity, solid frame anisotropy and tortuosity on the propagation of seismoelectric waves, five models (labelled B–F) with different parameters are presented in Table 1.

The difference between Models B and A is that Model A is isotropic, while B is anisotropic with non-zero Thomsen parameters. As a consequence, the values of the elastic components of the stiffness tensor are changed. Simulated results at 12 milliseconds are shown in Fig. 4. We observe that a transverse wave (S) with SV mode is generated in this anisotropic

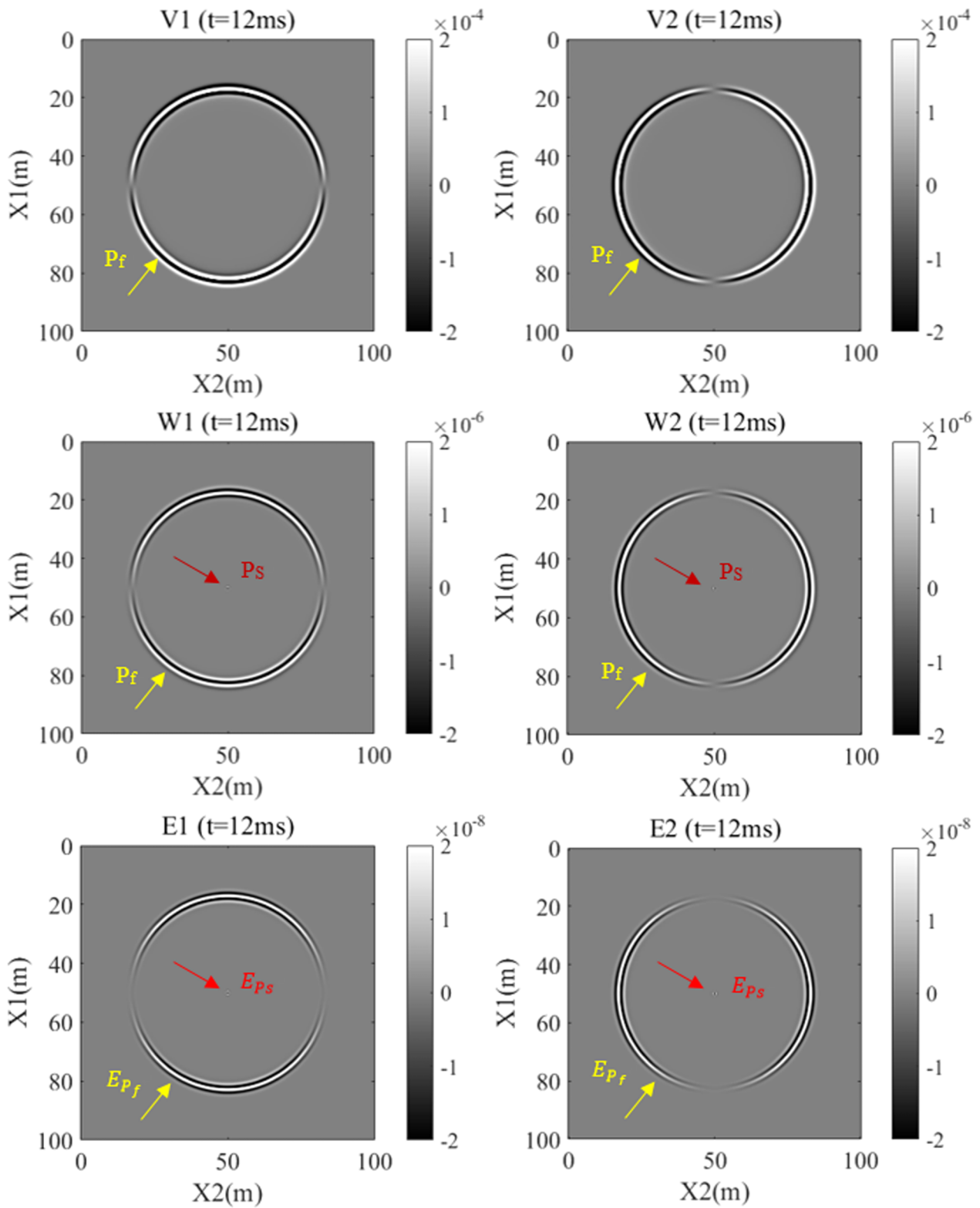


Figure 3 Seismoelectric snapshots of Model A showing solid velocity (top row), relative velocity (middle row) and electric field (bottom row). The vertical components are shown in the left column and the horizontal components in the right column.

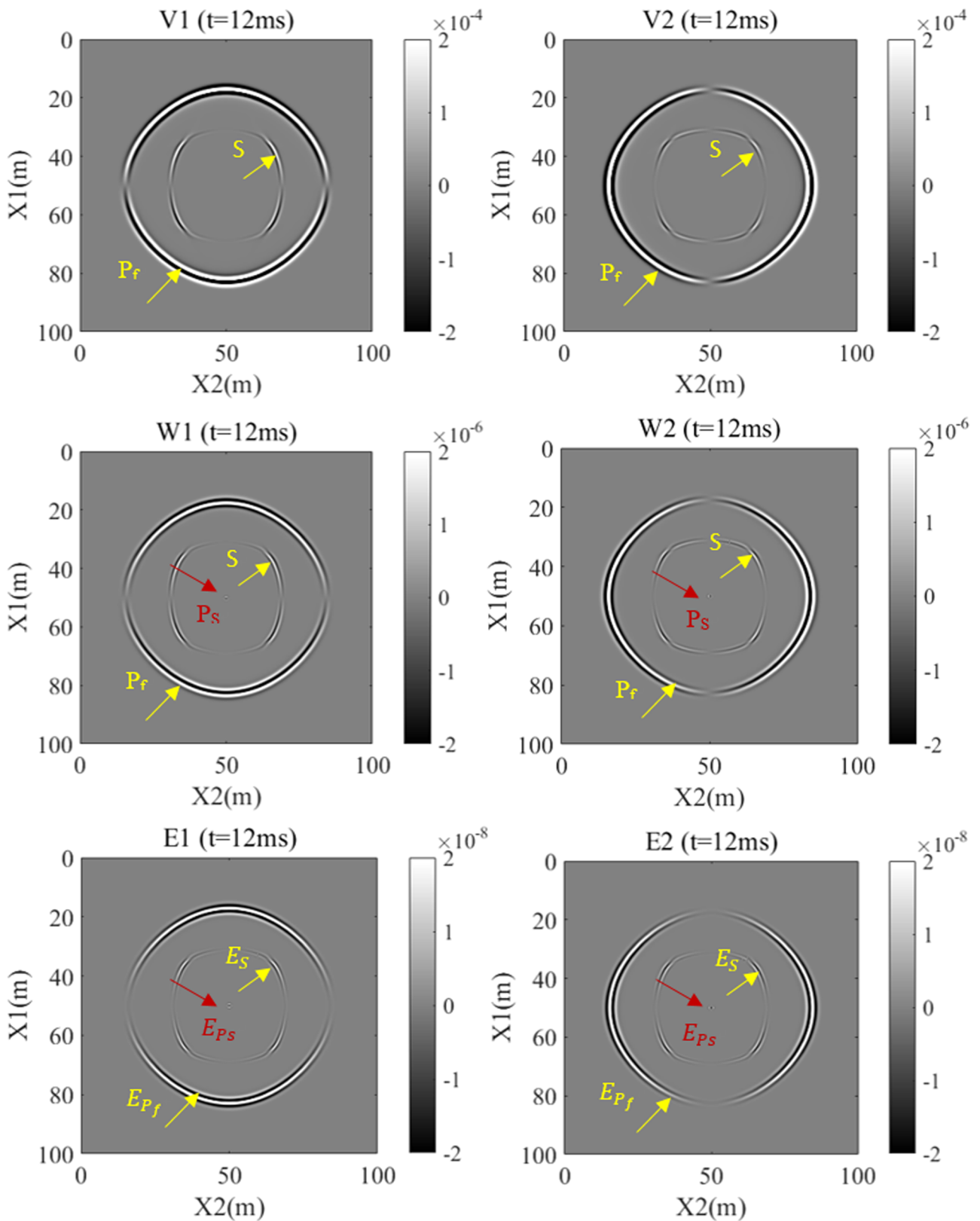


Figure 4 Seismoelectric snapshots of Model B showing solid velocity (top row), relative velocity (middle row) and electric field (bottom row). The vertical components are shown in the left column and the horizontal components in the right column.

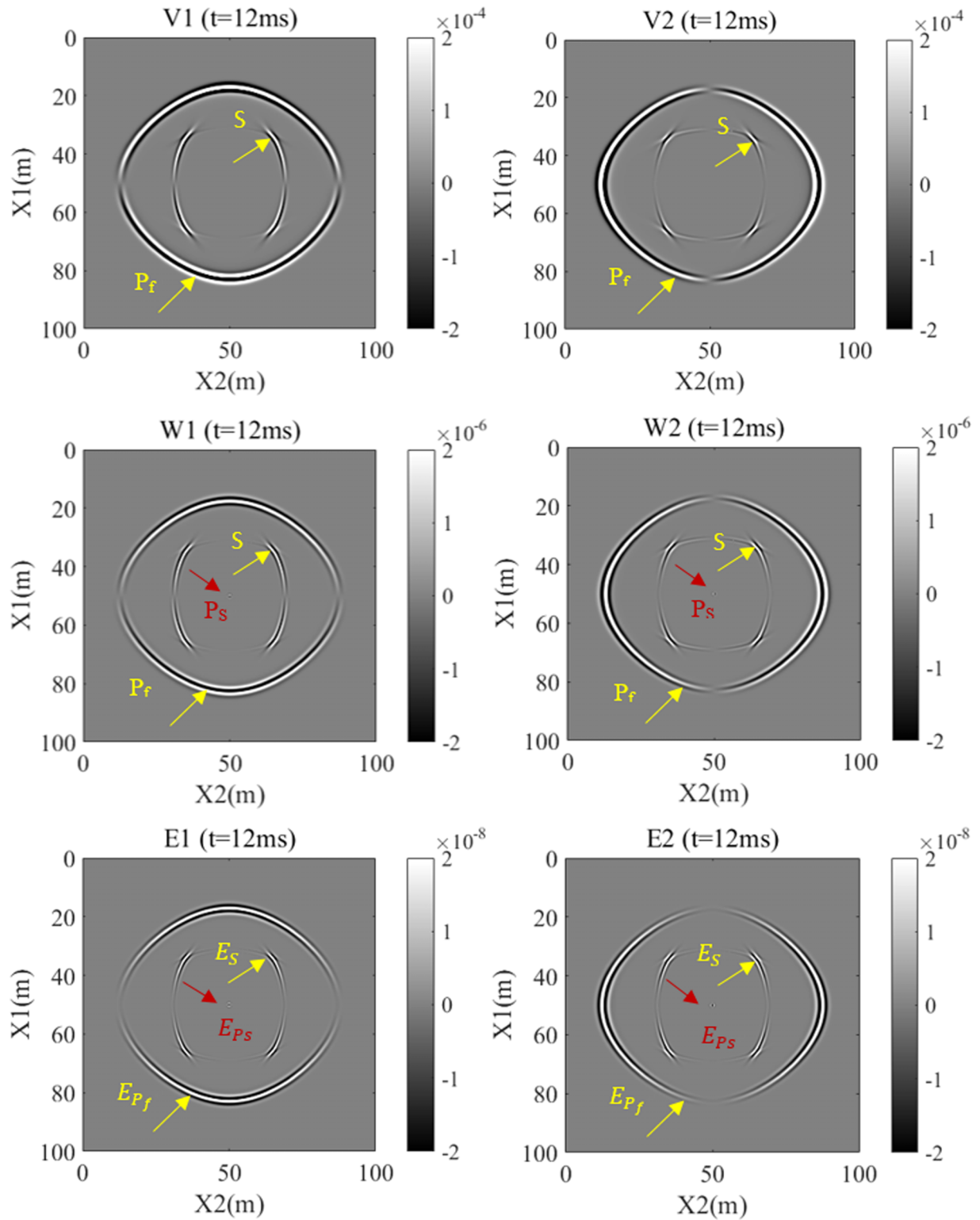


Figure 5 Seismoelectric snapshots of Model C showing solid velocity (top row), relative velocity (middle row) and electric field (bottom row). The vertical components are shown in the left column and the horizontal components in the right column.

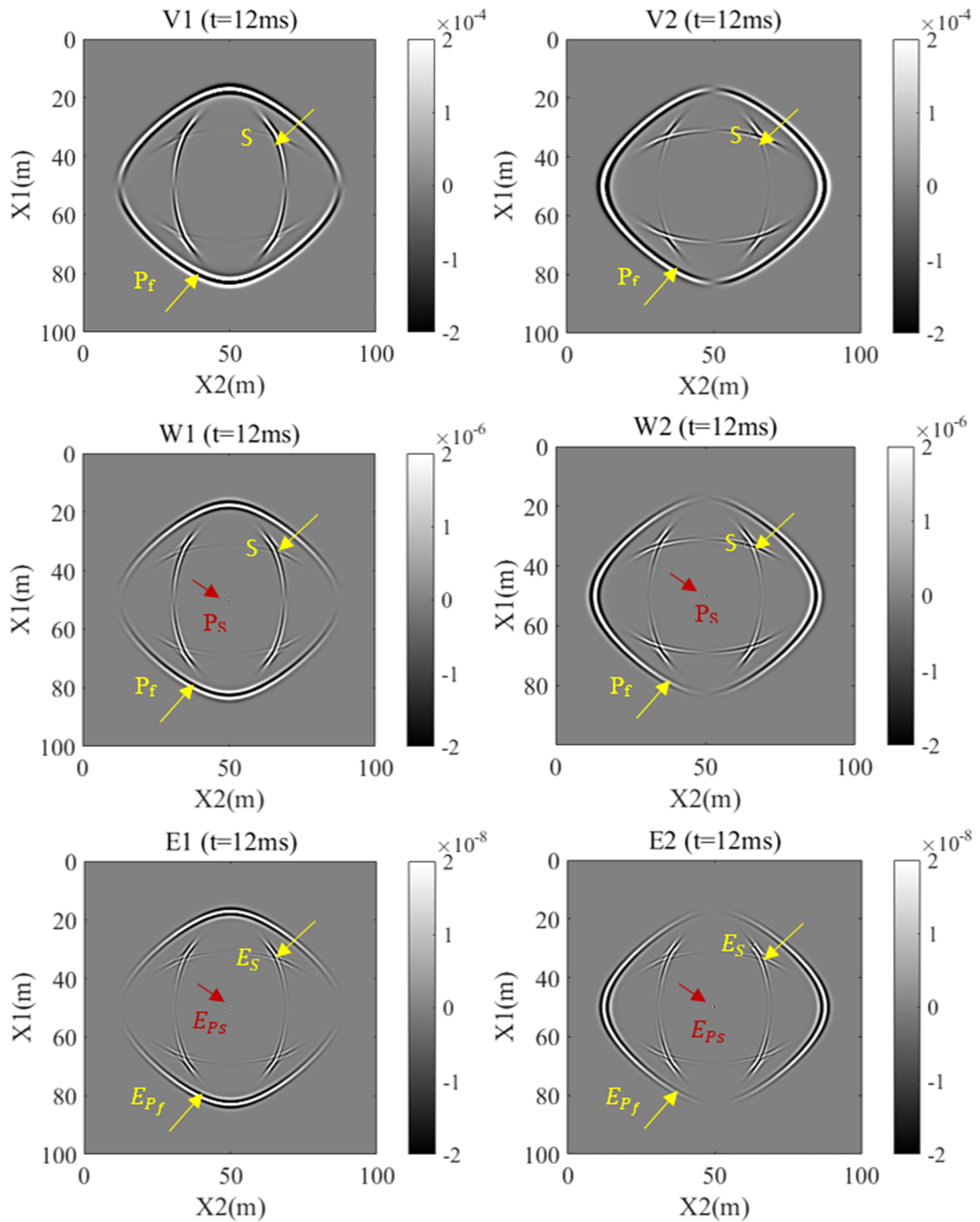


Figure 6 Seismoelectric snapshots of Model D showing solid velocity (top row), relative velocity (middle row) and electric field (bottom row). The vertical components are shown in the left column and the horizontal components in the right column.

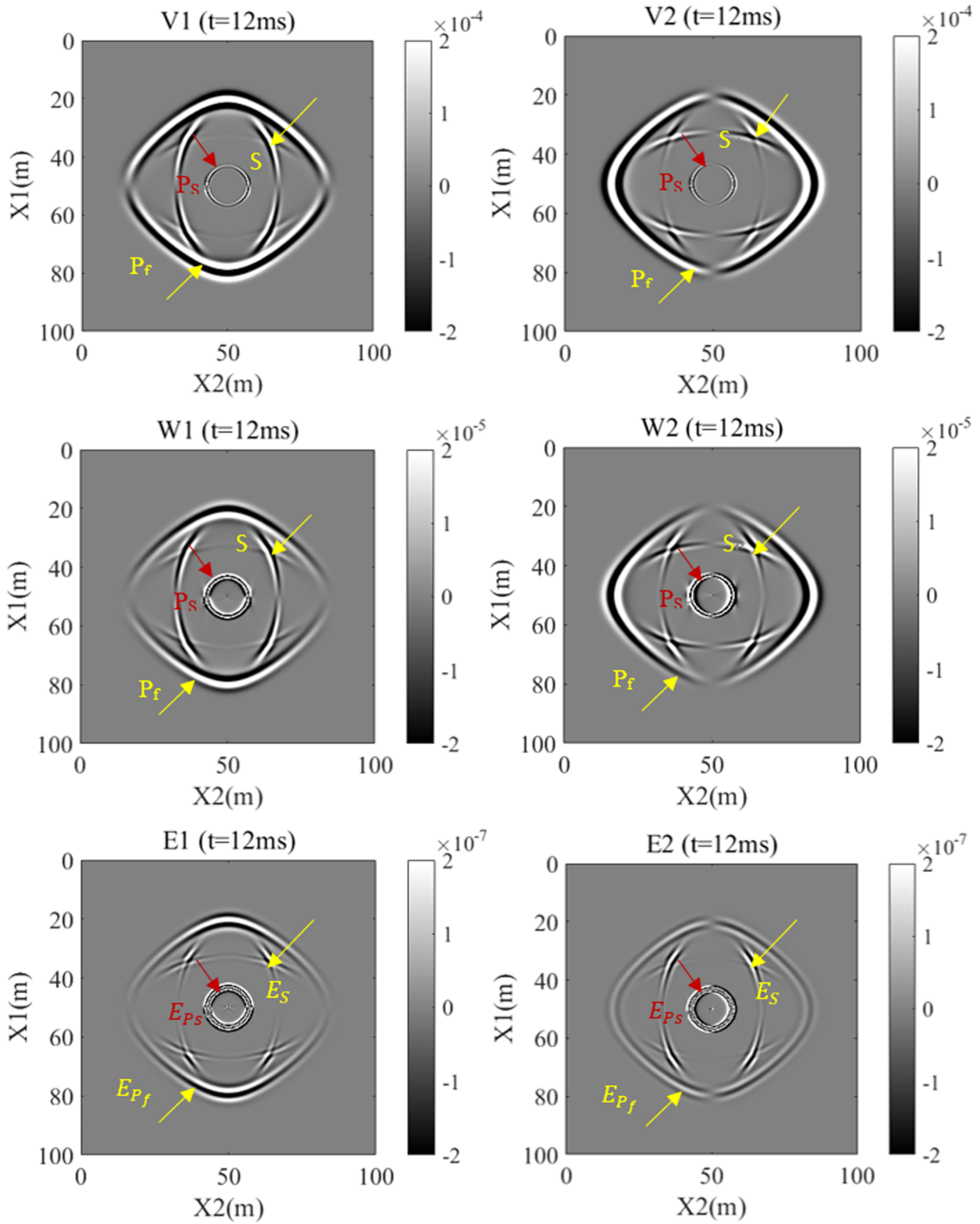


Figure 7 Seismoelectric snapshots of Model E showing solid velocity (top row), relative velocity (middle row) and electric field (bottom row). The vertical components are shown in the left column and the horizontal components in the right column.

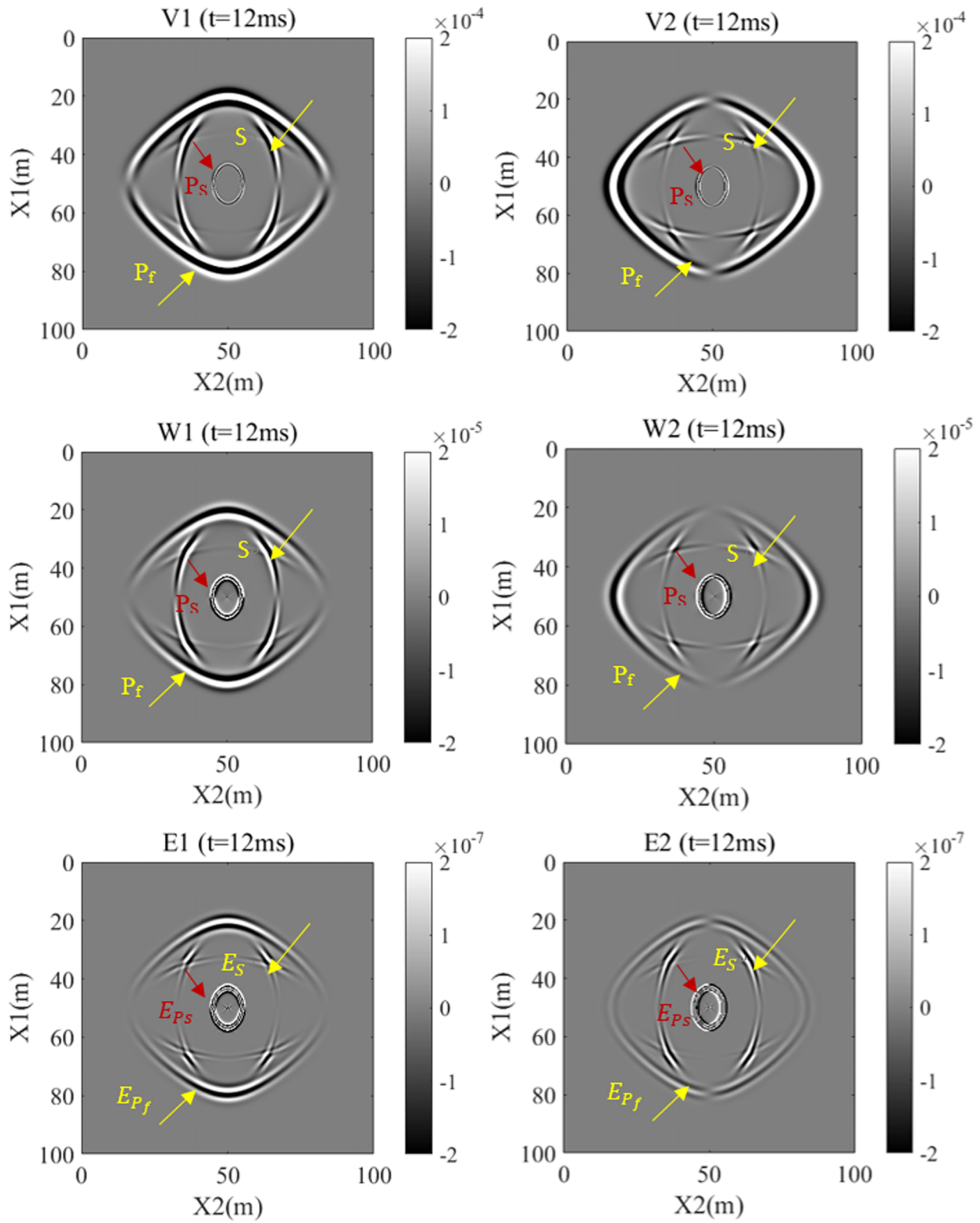


Figure 8 Seismoelectric snapshots of Model F showing solid velocity (top row), relative velocity (middle row) and electric field (bottom row). The vertical components are shown in the left column and the horizontal components in the right column.

Table 2 Computational time for different model sizes and different number of threads

Model Size	1 Thread	2 Threads	4 Threads	8 Threads	16 Threads
2000×2000	15 min and 19 s	9 min and 53 s	5 min and 9 s	3 min and 33 s	2 min and 58 s
4000×4000	60 min and 18 s	40 min and 3 s	20 min and 17 s	14 min and 24 s	11 min and 19 s

medium in addition to the fast and slow longitudinal waves in accordance with theory (Ben-Menahem and Sena, 1990; Ben-Menahem *et al.*, 1991). The coseismic electric field inside the S wave is denoted by E_S and its radiation pattern is that of the S wave. The reason of why there is an electric field accompanying the S wave is that the electric field is entirely determined by the divergence of the relative velocity under the quasi-static electric approximation. As soon as the seismic wave is present in the relative velocity and has a non-zero divergence. Equations (5), (6) and (8) show that the divergence of the relative velocity is determined by the divergence of the solid velocity and the time derivative of stress/pressure.

In order to analyse the effect of solid frame anisotropy on the propagation of seismoelectric waves, we simulate the seismoelectric response in Model C. The value of Thomsen parameter ε is different in Model C compared to Model B, so that we can analyse the effect of ε on the propagation of seismoelectric waves. Simulated results at 12 milliseconds are shown in Fig. 5. We observe from Fig 5 that the P_f waves of Model C show more anisotropy effects than the P_f waves of Model B. This result confirms that the value of Thomsen anisotropic parameter ε contributes more to the anisotropic behaviour of the P_f wave than of the S wave (Cai *et al.*, 2013; Wang *et al.*, 2018).

In order to analyse the effect of δ on the propagation of seismoelectric waves, we simulate the seismoelectric response in Model D. The difference between Models D and C is that the value of δ is different in Model D compared to Model C. Simulated snapshots at 12 milliseconds are shown in Fig. 6. We observe that two types of transverse waves (S) are separated from each other, in other words, S waves are split under the effect of δ . From this we confirm that δ contributes more to the anisotropy of the S wave than to the P wave (Cai *et al.*, 2013; Wang *et al.*, 2018).

In order to analyse the effect of fluid viscosity on the propagation of seismoelectric waves, we simulate the seismoelectric response in Model E. The difference between Models E and D is that the value of fluid viscosity is decreased in Model E. Simulated results at 12 milliseconds are shown in Fig 7. We observe that slow longitudinal wave (P_S) and the associated coseismic electric field (E_{P_S}) do not appear at source location

in the static mode anymore, but propagate through the model, in other words, the propagation speed of the slow longitudinal wave increases with decreasing fluid viscosity. From this we confirm that fluid viscosity has a large effect on the propagation of slow longitudinal wave and the associated coseismic electric field (E_{P_S}).

Finally, we simulate the seismoelectric response in Model F to analyse the effect of tortuosity on the propagation of seismoelectric waves. The difference between Models F and E is that the tortuosity is anisotropic in Model F. As a consequence, the coupling coefficient is anisotropic as well because it is inversely proportional to the tortuosity. As it can be seen in Guo (2012) that there exists a correlation between tortuosity and permeability, therefore the permeability in Model F is also anisotropic. We show the modelling results at 12 milliseconds in Fig. 8. We observe the oval shape in the snapshot of the slow longitudinal wave and its coseismic electric field (E_{P_S}), while they have circular shapes in the result of Model E. From this we confirm that tortuosity has an effect on the propagation of the slow longitudinal wave and its coseismic electric field (Cai *et al.*, 2013). In addition, we can observe from Figs 7 and 8 that the solid and relative velocity fields have opposite polarity, which also holds for the electric field and relative velocity. We can explain these polarity reversal from equations (1)–(4) and (9)–(11). Equations (1)–(4) show that the solid and relative velocity fields have opposite signs. The opposite sign of electric field and relative velocity field is observable from equations (9)–(11).

Only coseismic electric fields can be generated in a homogeneous medium. In order to study the propagation characteristics of interface responses in an anisotropic medium and analyse its sensitivity to contrasts in directional properties of the subsurface, we plan to simulate the wavefields in a layered medium and show results in the future.

Parallelizing efficiency

Our FDTD simulation program is parallelized based on a shared memory architecture using Open MP. We test the performance of parallel computing by running simulations for 20 milliseconds in a model with constant grid sizes, but with

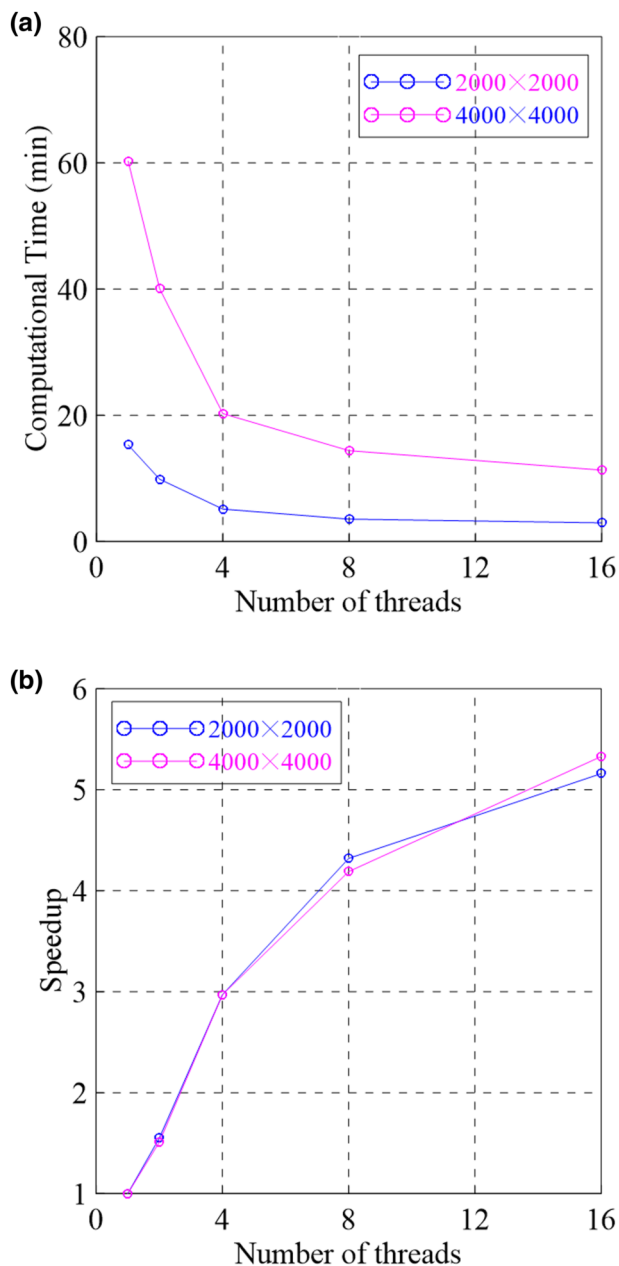


Figure 9 Variation of computational time and speed-up with the number of threads for different model sizes: (a) computational time and (b) speed-up.

varying the number of threads. The model size and number of threads are illustrated in Table 2. Based on Table 2, we can examine the parallel performance by analysing the speed-up and computational time as a function of the number of threads.

We show the parallel performance in Fig. 9. We observe that the computational time decreases and speed-up increases when the number of threads increases.

CONCLUSIONS

The coupling equations of seismoelectric waves in porous medium with electric isotropy and elastic anisotropy are developed by using a primary-secondary formulation. Based on the finite difference time domain (FDTD) algorithm, the propagation of seismoelectric waves are analysed in detail by computing snapshots. The simulation results show that four types of waves are generated in an anisotropic poroelastic medium, the fast longitudinal wave (P_f), slow longitudinal wave (P_s) and two split transverse waves. These four types of seismic waves generate coseismic electric fields in a homogenous anisotropic poroelastic medium. The fluid viscosity and medium tortuosity have an effect on the propagation of the slow longitudinal wave. The slow longitudinal wave propagates slowly under the influence of fluid viscosity, and the propagation speed increases with decreasing fluid viscosity. The snapshot shape of the slow longitudinal wave appears as oval when the tortuosity is anisotropic but circular when the tortuosity is isotropic. The anisotropy of P_f and S waves is more sensitive to the values of ε and δ , respectively.

ACKNOWLEDGEMENTS

We are very grateful to editor and two anonymous reviewers for their helpful suggestions. This work is supported by Key Research Program of Frontier Sciences, CAS, (Grant No. QYZDY-SSW-DQC009) and National Science and Technology Major Project of China (Grant No. 2017ZX05032-003-001).

ORCID

Munirdin Tohti  <https://orcid.org/0000-0003-0651-3184>

Evert Slob  <https://orcid.org/0000-0002-4529-1134>

REFERENCES

- Ben-Menahem, A., Gibson, R., Jr. and Sena, A. (1991) Green's tensor and radiation patterns of point sources in general anisotropic inhomogeneous elastic media. *Geophysical Journal International*, 107, 297–308.
- Ben-Menahem, A. and Sena, A. (1990) Seismic source theory in stratified anisotropic media. *Journal of Geophysical Research*, 95, 15395–15427.
- Bordes, C., Jouniaux, L., Dietrich, M., Pozzi, J. and Garambois, S. (2006) First laboratory measurements of seismo-magnetic conversions in fluid filled Fontainebleau sand. *Geophysical Research Letters*, 33. <https://doi.org/10.1029/2005GL024582>.
- Biot, M.A. (1955) Theory of elasticity and consolidation for a porous anisotropic solid. *Journal of Applied Physics*, 26, 182–185.

- Biot, M.A. (1956a) Theory of propagation of elastic waves in a fluid saturated porous medium. I. Low-frequency range. *Journal of Acoustical Society of America*, 28, 168–178.
- Biot, M.A. (1956b) Theory of propagation of elastic waves in a fluid saturated porous medium. II. Higher-frequency range. *Journal of Acoustical Society of America*, 28, 179–191.
- Biot, M.A. (1962) Mechanics of deformation and acoustic propagation in porous media. *Journal of Applied Physics*, 33, 1482–1498.
- Cai, L., Qi, G., Tian, L., Jie, Y., Huan, F., Qi, L., Yang, L., Dian, W. and You, T. (2013) *Numerical Simulation of Seismic Wave Field in Complex Medium*. Beijing: Sciences Press, pp. 73–78.
- Carcione, J. (1995) Wave propagation in anisotropic, saturated porous media: plane-wave theory and numerical simulation. *Journal of Acoustical Society of America*, 99, 2655–2667.
- Gao, Y. and Hu, H. (2009) Numerical simulation and analysis of seismoelectromagnetic wave fields excited by a point source in layered porous media. *Chinese Journal of Geochemistry*, 52, 2093–2104.
- Gao, Y. and Hu, H. (2010) Seismoelectromagnetic waves radiated by a double couple source in a saturated porous medium. *Geophysical Journal International*, 181, 873–896.
- Gao, Y., Huang, F. and Hu, H. (2017a) Comparison of full and quasi-static seismoelectric analytically based modelling. *Journal of Geophysical Research*, 122, 8066–8106.
- Gao, Y., Huang, F. and Hu, H. (2017b) Seismoelectric responses to an explosive source in a fluid above a fluid saturated porous medium. *Journal of Geophysical Research*, 122, 7190–7218.
- Gao, Y., Wang, D., Yao, C., Guan, W., Hu, H., Wen, J., Zhang, W., Tong, P. and Yang, Q. (2018) Simulation of seismoelectric waves using finite-difference frequency-domain method: 2-D SHTE mode. *Geophysical Journal International*, 216, 414–438.
- Garambois, S. and Dietrich, M. (2001) Seismoelectric wave conversions in porous media: field measurements and transfer function analysis. *Geophysics*, 66(5), 1417–1410.
- Garambois, S. and Dietrich, M. (2002) Full waveform numerical simulation of seismoelectromagnetic wave conversions in fluid-saturated porous media. *Journal of Geophysical Research: Solid Earth*, 107, ESE 5-1 to ESE 5-18.
- Gilbert, R. and Shoushani, M. (2017) The Biot model for anisotropic poro-elastic media: the viscoelastic fluid case. *Journal of Computational Acoustics*, 25. <https://doi.org/10.1142/S0218396X17500126>.
- Guo, P. (2012) Dependency of tortuosity and permeability of porous media on directional distribution of pore voids. *Transport in Porous Media*, 95: 285–303.
- Haartsen, M. and Pride, S. (1997) Electro seismic waves from point sources in layered media. *Journal of Geophysical Research*, 102, 24745–24769.
- Haines, S. and Pride, S. (2006) Seismoelectric numerical modelling on a grid. *Geophysics*, 71(6) N57–N65.
- Ivanov, A. (1939) Effect of electrization of earth layers by elastic waves passing through them. *Doklady Akademii Nauk SSSR*, 24, 42–25.
- Jardani, A. and Revil, A. (2015) Seismoelectric couplings in a poroelastic material containing two immiscible fluid phases. *Geophysical Journal International*, 202, 850–870.
- Martner, S. and Sparks, N. (1959) The electro seismic effect. *Geophysics*, 24(2), 297–308.
- Mikhailov, O.V., Haartsen, M.W. and Toksoz, M.N. (1997) Electro seismic investigation of the shallow subsurface: field measurements and numerical modelling. *Geophysics*, 62(1), 97–105.
- Petropoulos, P., Li, Z. and Cangelaris, C. (1998) A reflectionless sponge layer absorbing boundary condition for the solution of Maxwell's equations with high-order staggered finite difference schemes. *Journal of Computational Physics*, 139, 184–208.
- Pooladi, A., Rahimian, M. and Pak, R. (2017) Poroelastodynamic potential method for transversely isotropic fluid – saturated poroelastic media. *Applied Mathematical Modelling*, 50, 177–199.
- Pride, S. (1994) Governing equations for the coupled electromagnetic sand acoustics of porous media. *Physical Review B*, 50, 15678–15696.
- Pride, S. and Haartsen, M. (1996) Electro seismic wave properties. *Journal of the Acoustical Society of America*, 100, 1301–1315.
- Ren, H., Chen, X. and Huang, Q. (2011) Numerical simulation of coseismic electromagnetic fields associated with seismic waves due to finite faulting in porous media. *Geophysical Journal International*, 188, 925–944.
- Ren, H., Huang, Q. and Chen, X. (2016) Numerical simulation of seismoelectromagnetic fields associated with a fault in a porous medium. *Geophysical Journal International*, 206, 205–220.
- Revil, A. and Linde, N. (2006) Chemico-electromagnetical coupling in microporous media. *Journal of Colloid and Interface Science*, 302, 682–694.
- Revil, A. and Mahardika, H. (2013) Coupled hydromechanical and electromagnetic disturbances in unsaturated porous materials. *Water Resources Research*, 49, 744–766.
- Schakel, M.D., Smeulders, D.M.J., Slob, E.C. and Heller, H.K.J. (2011a) Laboratory measurements and theoretical modelling of seismoelectric interface response and coseismic wave fields. *Journal of Applied Physics*, 109. <https://doi.org/10.1063/1.3567945>.
- Schakel, M.D., Smeulders, D.M.J., Slob, E.C. and Heller, H.K.J. (2011b) Seismoelectric interface response: experimental results and forward model. *Geophysics*, 76(4), N29–N36.
- Schakel, M.D., Smeulders, D.M.J., Slob, E.C. and Heller, H.K.J. (2012) Seismoelectric fluid/porous medium interface response model and measurements. *Transport in Porous Media*, 93, 271–282.
- Schoemaker, F.C., Grobbe, N., Schakel, M.D. and Ridder, S.A.L. (2012) Experimental validation of electrokinetic theory and development of seismoelectric interferometry by cross-correlation. *International Journal of Geophysics*. <https://doi.org/10.1155/2012/514242>.
- Sharma, M. (2007) Wave propagation in a general anisotropic poroelastic medium: Biot's theory and homogenization theory. *Journal of Earth System Science*, 116, 357–367.
- Slob, E. and Mulder, M. (2016) Seismoelectric homogeneous space Green's function. *Geophysics*, 81(4), F27–F40.
- Thompson, A.H., Hornbostel, S., Burns, J., Murray, T., Raschke, R., Wride, J., McCammon, P., Sumner, J., Haake, G., Bixby, M., Ross, W., White, B.S., Zhou, M. and Peczak, P. (2007) Field test of electro seismic hydrocarbon detection. *Geophysics*, 72(1), N1–N9.

- Thomsen, L. (1986) Weak elastic anisotropy. *Geophysics*, 51(10), 1954–1966.
- Tsvankin, L. (1996) P-wave signatures and notation for transversely isotropic media: an overview. *Geophysics*, 61(2), 467–483.
- Tsvankin, L. (1997) Anisotropic parameters and P-wave velocity for orthorhombic media. *Geophysics*, 62(4), 1292–1309.
- Virieux, J. (1984) Sh-wave propagation in heterogeneous media-velocity-stress finite-difference method. *Geophysics*, 49(11), 1933–1942.
- Wang, Y., Mu, P., Duan, Y. and Wang, T. (2018) Numerical simulation of elastic wave equation and analysis of wave field characteristics in 2-D VTI medium. *Open Journal of Yangtze Gas and Oil*, 3, 153–166.
- White, B.S. and Zhou, M. (2006) Electro seismic prospecting in layered media. *Society for Industrial and Applied Mathematics*, 67, 69–98.
- Yang, D.H. and Zhang, Z.J. (2002) Poroelastic wave equation including the Biot/Squirt mechanism and the solid/fluid coupling anisotropy. *Wave Motion*, 35, 223–245.
- Yee, K. (1966) Numerical simulation of initial boundary value problems involving Maxwell's equations in isotropic media. *IEEE Transactions on Antennas and Propagation*, 14, 302–307.
- Zhu, Z., Haartsen, M. and Toksöz, M.N. (1999) Experimental studies of electrokinetic conversions in fluid saturated borehole models. *Geophysics*, 64(5), 1349–1356.
- Zhu, Z. and Toksöz, M.N. (2013) Experimental measurements of the streaming potential and seismoelectric conversion in Berea sandstone. *Geophysical Prospecting*, 61, 688–700.
- Zhu, Z. and Toksöz, M.N. (2015) Seismoelectric measurements in a porous quartz-sand sample with anisotropic permeability. *Geophysical Prospecting*, 64, 700–713.
- Zhu, Z., Toksöz, M.N. and Burns, D. (2008) Electro seismic and seismoelectric measurements of rock samples in a water tank. *Geophysics*, 73(5), E153–E164.
- Zyserman, F., Gauzellino, P. and Santos, J. (2010) Finite element modelling of SHTE and PSVTM electroseismics. *Journal of Applied Geophysics*, 72, 79–91.